Journal of Manufacturing Processes 89 (2023) 314–327

Contents lists available at ScienceDirect

Journal of Manufacturing Processes

journal homepage: www.elsevier.com/locate/manpro

On the melt pool dynamic of voxel-controlled metal matrix composites via hybrid additive manufacturing: Laser powder bed fusion and ink-jetting

Milad Ghayoor [a,b], Omid Sadeghi [c], Bryce Cox [a], Joshua Gess [a], Somayeh Pasebani [a,b,*]

[a] School of Mechanical, Industrial and Manufacturing Engineering, Oregon State University, Corvallis, OR 97330, United States of America
[b] Advanced Technology and Manufacturing Institute (ATAMI), Corvallis, OR 97330, United States of America
[c] Phosio Corporation, Corvallis, OR 97330, United States of America

ARTICLE INFO

Keywords:
Metal matrix composite
Hybrid additive manufacturing
Ink-jetting
Laser powder bed fusion
Nanocluster
316L

ABSTRACT

In this study, the effect of the addition of reinforcement nanoparticles to the 316L matrix by adopting ex-situ and in-situ method (drop on demand jetting) to produce 316L/Al_2O_3 nanocomposite was investigated. In the ex-situ method, the Al_2O_3 nanoparticles (NPs) were lightly mixed with 316L powder and processed by laser powder bed fusion. In the in-situ method, an ethanol-based ink containing Al_{13} nanoclusters (NCs) was added to 316L powder and then processed by laser. Both ex-situ and in-situ method produced nanocomposites with Al-Si-Mn-O-enriched precipitations within the 316L matrix. The addition of NPs/NCs to the 316L matrix, altered the geometrical characteristic of the single-track melt pools. At the same laser power, with increasing the amount of Al_2O_3 NPs and Al_{13} NCs the melt pool deepened due to reduced thermal conductivity and prolonged liquid presence. As a result, 316L/1 wt% Al_{13} NCs deposited single track showed larger grains in comparison to 316L single track. At a high laser power of 150 W, the Marangoni flow and the buoyancy force caused the nanoparticles to agglomerate and float to the top surface of tracks; therefore, the wt% fraction of precipitation was drastically reduced due to the loss of Al. The 316L/Al_2O_3 NPs and 316L/Al_{13} NCs exhibited the microhardness of 285 ± 13 HV and 293 ± 7 HV, respectively, higher than the deposited 316L single track, 265 ± 15 HV. Lastly, a hybrid LPBF+ink-jet printer was adopted to selectively change the composition of different zones by adding Al_{13} NCs ink to 316L and producing a voxel-controlled metal matrix composite.

1. Introduction

Particle reinforced metal matrix composites (MMCs) are increasingly employed in aerospace, automotive, and power plants as structural materials due to their excellent combination of high strength, thermal stability, and ductility [1,2]. Metal matrix nanocomposites (MMNCs) are a type of MMCs in which the matrix is reinforced with nanoparticles; giving superior mechanical properties for many applications over MMCs [3,4]. The conventional manufacturing of MMNCs can be categorized into two types; solid-state methods such as powder metallurgy, mechanical alloying [5], spark plasma sintering [6], and liquid-state methods including stirring casting [7]. Nanoparticles are prone to agglomerate into coarsened clusters due to their poor wettability with the molten matrices and large Van der Waals' force, making homogeneous dispersion extremely challenging and subsequent thermo-mechanical treatment is not effective in eliminating these drawbacks [8]. Recently, new technologies of high energy like metal additive manufacturing have been utilized to well-dispersed reinforcement nanoparticles in MMNCs and achieve microstructural homogeneity and improve mechanical properties in a net shape part [9,10].

The laser powder bed fusion (LPBF) process is a metal additive manufacturing process with the advantages of fabricating freeform geometries and ultrafine and gradient microstructure attributed to rapid melting and solidification [11–13]. During the LPBF process, a laser selectively scans a layer of metal powder deposited onto a build plate according to the sliced computer-aided design (CAD) model. Upon absorption of the laser irradiation, the scanned powders are melted and then quickly solidify, giving rise to the formation of a single track. The as-fabricated samples are then produced by repeating such a process in a layer-by-layer manner. Yadroitsev et al. [14] analyzed the formation of a single track from metal powder by LPBF process and stated that the performance of a component built by LPBF largely depends on the

* Corresponding author at: School of Mechanical, Industrial and Manufacturing Engineering, Oregon State University, Corvallis, OR 97330, United States of America.
E-mail address: Somayeh.Pasebani@oregonstate.edu (S. Pasebani).

https://doi.org/10.1016/j.jmapro.2023.01.059
Received 4 October 2022; Received in revised form 28 December 2022; Accepted 22 January 2023
Available online 3 February 2023
1526-6125/© 2023 The Society of Manufacturing Engineers. Published by Elsevier Ltd. All rights reserved.

quality of each deposited single track and every single layer. Sound single tracks well bonded to the substrate/previous layer are required to obtain a qualified part. Furthermore, to produce a single layer, the optimized hatch spacing should be considered to remelt the portion of the former single track to produce a metallurgical bond between two adjacent single tracks. Essentially, the hatch spacing determines the overlapping rate between adjacent tracks. Therefore, it can be reasonably assumed that, since LPBF is a track-by-track and layer-by-layer process, the performance of a component built by LPBF process strongly depends on each single track properties such as formability, dimension, and microstructure of deposited single track. [15].

Since the property of single track would determine the final printed part quality, researchers have focused on LPBF processing parameters optimization and understanding of the fundamental of laser beam absorption, melt flow, spattering, and denudation zone based on single track deposition on Fe-, Ti-, Ni- and Al-based alloys [14,16,17]. While most studies focused on the process optimization, microstructure characterization, and modeling of bulk MMNCs produced with LPBF, limited attention has been paid to the fundamental understanding of the underlying physics of the LPBF process of producing MMNCs. For example, AlMangour [18–20] reported densification behavior, microstructural evolution, and mechanical properties of TiC/316L [18], TiB_2/316L [19], and TiC/H13 [20] prepared by ball milling and LPBF process. However, there is a fundamental gap in understanding the single-track behavior of MMNCs, such as how the nanoparticles would influence the melt pool geometry, alter thermo-physical properties, melt pool flow, and eventually the microstructure and properties of the MMNCs. Furthermore, to the best knowledge of authors, the role of nanoparticles and process parameters on the redistribution and size of nanoparticles has not been addressed in the current literature.

Nanocomposite powder feedstock is not commercially available for LPBF process, and various preparation methods have been utilized to mix the second phase nanoparticles and matrix powders such as direct mixing, high-energy ball milling, agent deposition, and electrodeposition [21–24]. In direct mixing which is the simplest method, second-phase nanoparticles are distributed around the matrix powder surface and maintain spherical morphology/good flowability. However, nanoparticle agglomeration and poor wettability are disadvantages of this method [22]. Ball milling is the most popular method to avoid agglomeration of nanoparticles, however, it changes powder morphology and reduces flowability, and is a very time-consuming and costly process with no potential for scale-up [22]. Therefore, other alternative approaches for manufacturing MMNCs are receiving considerable attention among researchers with a focus on achieving both scalability and consistent properties [25,26].

In theory and practice, adding second phase reinforcement using the directed energy deposition (DED) process for making a multi-component material is feasible by blowing a second phase powder into a melt pool to form MMC [27]. However, DED has several limitations, such as the formation of intermetallic phases and low dimensional accuracy. These limitations do not exist in the LPBF process in which metal powder is spread in layers and locally melted with a laser heat source. Technical and cost challenges to selectively adding reinforcement nanoparticles to a powder bed are preventing AM of multi-functional multi-materials. Indeed, current LPBF methods are limited to making only single material components and producing MMCs using premixed precursor powder and reinforcement particles [28,29]. Therefore, novelty of this work is producing multi-functional multi-material using drop on demand in LPBF process.

In this study, a novel approach is presented that is intended to revolutionize the use of LPBF as a means of voxel-controlling the composition to achieve targeted properties, and also eliminate the need for ball milling in manufacturing of 316L/Al_2O_3 nanocomposite. In this sense, a hybrid of LPBF and ink-jetting machine has been developed at Oregon State University; which allows nanoparticles to be embedded into a powder bed via a drop-on-demand approach. Our approach was to incorporate a jetting module into an LPBF machine build chamber and dispense the nanoparticles being carried in the form of ink, to the powder bed and in-situ additive manufacture MMNCs without any prior ball milling. To the best of our knowledge, there is no mechanism available in the LPBF process to make MMNCs. This hybrid tool would enable us to spatially vary the composition by changing the solid loading using ink to the matrix. Furthermore, this approach could be further enhanced by employing a different ink composition and concentration to vary the material properties throughout components. Thus, it is of great importance to fill the fundamental knowledge gap on the role of adding nanoparticles to the melt pool. In doing so, single-track experiment has been designed to evaluate the influence of the addition of nanoparticles onto the melt pool and microstructure evolution of a MMNC. The detailed evaluation of the microstructure and nanoparticles evolution during the MMNCs manufacturing process is fundamental to understanding the role of nanoparticles in every step of the process. In future work, the control of the process is necessary for the adoption of this in-situ technique to produce MMNCs with targeted properties otherwise known as functionally graded alloys (FGAs).

2. Experimental procedure

2.1. Powder preparation and characterization

Gas atomized 316L stainless steel powder was procured from Carpenter Additive with the chemical composition provided in Table 1. The 316L powders were mixed with 1, 2.5, and 5 wt% of Al_2O_3 particles in a planetary ball mill (Retsch, PM100). The Al_2O_3 was procured from US Research Nanomaterial with nearly spherical morphology, purity of +99 %, and particle size of 20 nm. The rotation speed of 100 rpm, mixing time of 4 h, and ball-to-powder ratio of 1:1 was used in ball milling.

Fig. 1(a) shows the morphology of 316L stainless steel powder; the powder has a spherical morphology with a finer satellite attached to the larger particles. Fig. 1(b)-(c) shows the SEM micrograph of mixed 316L + 1 wt% Al_2O_3 and 316L + 5 wt% Al_2O_3 powder, respectively. After 4 h of light ball milling, powder morphology remained unchanged and did not experience a severe deformation or irregularity. The inset in Fig. 1 (b)-(c) demonstrates the surface of 316L powder after mixing; showing the Al_2O_3 nanoparticles uniformly covered the outer surface of 316L powder.

2.2. Nanocluster ink preparation

Nanoclusters (NCs) contain two or more metal cations with aqua (H_2O), Oxo (O^{2-}), hydroxo ligands, or a combination of them. These clusters are smaller than nanoparticles but larger than an atom, on the 0–2 nm scale, and they are considered to be an intermediate step for the formation of nanoparticles. In this study, NCs of Al_{13} were synthesized according to the procedure reported in Ref. [30]. Further details about NCs and why they were used in this study can be found in the Supplementary data section. Next, an ethanol-based ink was prepared by dissolving 10 wt% of Al_{13} NCs in ethanol. According to the reaction Eq. (1), the heated Al_{13} NC converts to Al_2O_3 and gases which eventually gets mixed with the nitrogen atmosphere in the LPBF chamber. To check the feasibility of forming Al_2O_3 after laser treatment, 100 g of Al_{13} NCs ink were heated up in a box furnace in the air to the maximum temperature of 1000 °C, and after that XRD analysis was performed on the remaining powder. As shown in Supplementary Fig. 3, the resulted powder contained an alumina phase implying that Al_{13} NCs were converted to Al_2O_3 particles during the LPBF process.

$$4\left[Al_{13}(OH)_{24}(H_2O)_{24}\right](NO_3)_{15} + \text{Laser (Heat)} \rightarrow 26\ Al_2O_3 + 144\ H_2O + 60\ NO_2 + 15O_2 \quad (1)$$

Table 1
Chemical composition of 316L stainless steel powder.

Element	Fe	Ni	Cr	Mo	C	Si	Mn	P	S	N	O
wt%	Bal	12.5	17.8	2.36	0.017	0.64	0.74	0.007	0.004	0.09	0.03

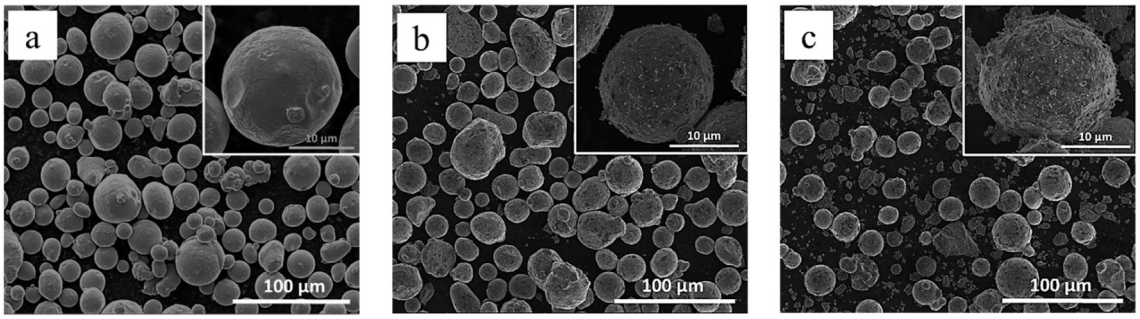

Fig. 1. SEM micrograph of (a) 316L stainless steel powder, (b) mixed 316L + 1 wt% Al_2O_3, and (c) mixed 316L + 5 wt% Al_2O_3, the insets demonstrate the surface of 316L particles coated with brighter Al_2O_3 nanoparticles.

2.3. Single-track experiment setup

In order to investigate the feasibility of making 316L nanocomposite using the ink-jetting approach, a single-track experiment was conducted to simulate the hybrid process and evaluate the microstructure before using the hybrid LPBF+Ink-jetting printer. The single-track experiment setup was conducted on a 316L stainless steel build plate with a dimension of 75 × 75 × 3 mm. In order to avoid the ink to spread across the plate and to maintain a constant layer thickness, a micro-groove with the dimensions of 12 mm in length, 200 ± 20 µm in width, and 50 ± 10 µm in depth was micromachined into the 316L build plate, as shown in Fig. 2(a). A Zygo Zescope was utilized to measure the dimension of micro-grooves as shown in Fig. 2(b). At least 20 grooves were measured and the average was reported above.

In the first stage of the single-track experiment, the 316L powder was spread on top of the groove to fill the entire groove, and a smooth surface on the top of the groove was manually achieved with the aid of a razor blade as shown in the inset of Fig. 2(a). Before melting, the laser beam was precisely aligned with the center of the groove to assure the single track will be formed in the center of the groove. Next, the powder layer was melted with the laser in the LPBF machine. The single-track deposition, as shown in Fig. 2(c), was performed in an OR Creator LPBF machine with a 250 W Yb: YAG fiber laser with a wavelength of 1067 nm. The oxygen level in the build chamber was kept at <100 ppm to minimize oxidation during the laser melting process. The laser power varied from 50 to 150 W with an increment of 25 W (total of 5 laser power variations). The scan speed of the laser was maintained constant at 200 mm/s.

In the second stage, the same procedure was repeated for producing 316L/Al_2O_3 nanocomposite by spreading the 316L powder mixed with 1, 2.5, and 5 wt% of Al_2O_3 nanoparticles, respectively, and producing single track 316L/Al_2O_3 nanocomposite. For this stage, all the laser

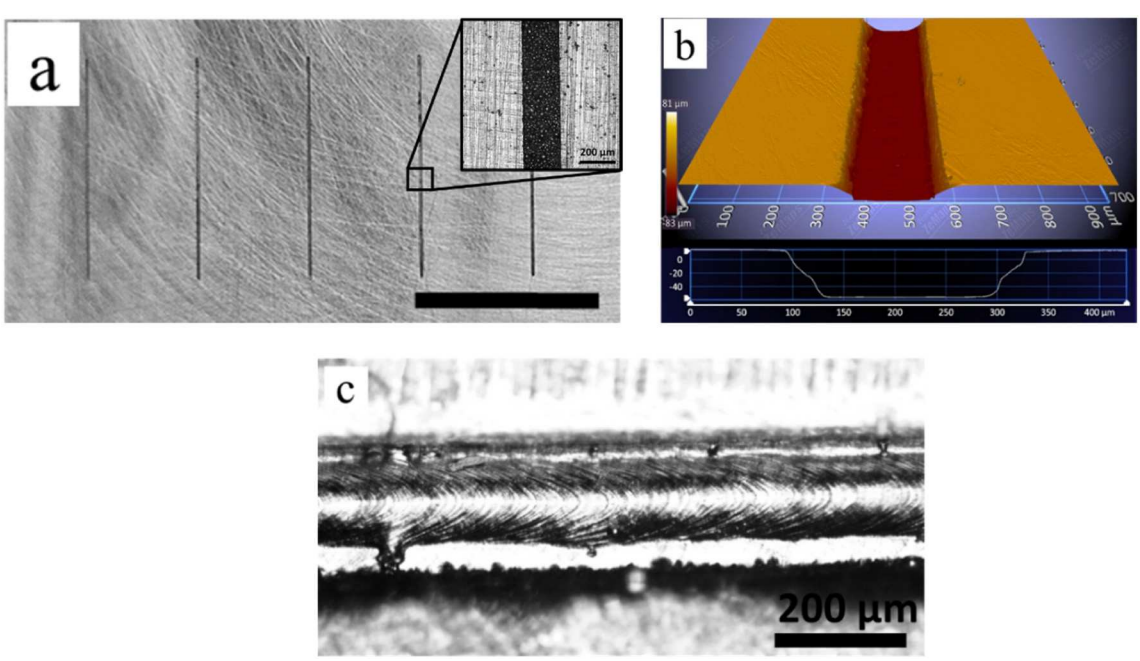

Fig. 2. (a) The grooves micromachined into the 316L build plate for depositing single tracks and maintaining the ink in the groove, the inset showing the groove after layering of powder, (b) 3D profile of a groove obtained from Zescope, and (c) deposited single track in the center of the groove.

process parameters were adopted from the first phase.

In the third stage, ink jetting was mimicked by adopting a micropipette to transfer the ink to the metal powder to manufacture 316/Al_2O_3 nanocomposite single tracks. According to the mass of metal powder in the groove, the Al_{13} NCs ink was prepared with the defined concentration of Al_{13} NCs to yield the targeted wt% of nanoparticles (1, 2.5, and 5 wt%) in the produced single-track nanocomposite. For this calculation, it was assumed that the conversion of Al_{13} NCs to Al_2O_3, is 100 %.

Using a micropipette, two 0.1 μL-droplets of the Al_{13} NCs ink were deposited at the start and end points of the groove to fill the entire groove via capillary action flow. The concentration of Al_{13} NCs varied through the experiment to yield targeted wt% of nanoparticles (1, 2.5, and 5 wt%) without changing the volume and number of droplets. In another word, to be consistent in the experimental procedure, the solids loading of the ink has been adjusted to yield the targeted wt% in the deposited single track. After depositing the ink, the plate was heated on a hot plate to the temperature of 100 °C, for 10 s to evaporate the ethanol and dry the Al_{13} NCs ink. Afterward, a layer of 316L powder was spread on the groove, and the laser melted the layer and produced a sandwich of 316L base plate/Al_{13} NCs/316L powder to make the 316L/Al_{13} NCs nanocomposite. For this phase, all the laser process parameters were adopted from the first phase.

2.4. Sample preparation and characterization methods

A total of 35 single tracks were deposited on the 316L substrates. Deposited single tracks were sectioned along the build direction (Z direction) and polished following standard metallography procedure. Before the examination, the prepared cross-sections were electroetched using a solution of 10 wt% oxalic acid-90 wt% deionized water at 15 V DC for 15 s. After electroetching, the measurements of depth, width, and height of the weld pools were carried out on an optical microscope (Zeiss, Axiotron). Detailed characterization was carried out on an FEI Quanta 3D scanning electron microscopy (SEM). In addition, electron backscattered diffraction (EBSD) was used to measure the grain size of the cross-section of single tracks. EBSD samples were polished in a vibratory polisher for 8 h using a 50 nm diamond slurry. A focused ion beam (FIB) was used to prepare a lamella from the single tracks on a FEI Helios 650 ultra-resolution dual beam. A transmission electron microscope (TEM), model FEI TITAN 80–200 equipped with ChemiSTEM technology, was used to examine the microstructure of prepared lamella and identify the nanoparticles in the matrix. A Leco microhardness tester (M-400A) at a load of 10 g was used to measure the microhardness values of the single track samples. All the indent measurements were conducted using SEM to mitigate the uncertainty of reading values of indent diagonal length in optical microscopy.

3. Results and discussions

3.1. Track geometry

Fig. 3(a)-(c) presents the geometry of melt pools of deposited single tracks of 316L, 316L + 1 wt% Al_2O_3 NPs and 316L + 1 wt% Al_{13} NCs, respectively. Laser power was maintained at 100 W for all samples. Significant changes in the geometry of melt pools were observed after adding Al_2O_3 NPs (Fig. 3b) and Al_{13} NCs (Fig. 3c). This is because thermo-physical properties (such as thermal conductivity, viscosity, and surface tension) of the matrix (316L here) were disrupted after the addition of NPs and NCs [31,32]. The role of the addition of Al_2O_3 NPs and Al_{13} NCs on the melt pool shape was investigated; the height, width, and depth of cross-sections of melt pools were measured at 5 random locations of single tracks (far from starting and ending points), and average values were reported.

Supplementary Fig. 4 presents the single-track height as a function of laser power and concentration of second phase reinforcement NPs/NCs, respectively. It was found that the track height was independent of laser power. A previous study conducted by Li et al. [33] on track heights of deposited single tracks of Inconel 625 was in agreement with our study. Furthermore, our study showed that track height in the deposited single track is also independent of the addition of NPs and NCs.

In an attempt to identify the role of NPs and NCs on the melt pool geometry, single-track width was measured and presented as a function of laser power and wt% of the second phase in Fig. 4(a)-(b), respectively. The width of melt pools increased at higher laser powers, and this clear trend was observed for all the single tracks with varying the wt% and form of second phase reinforcements. This trend implied the NPs/NCs did not have any significant effect on the width of melt pools as compared to laser power. Higher laser power led to higher volumetric energy density (VED) [34], higher melt pool temperature, and less surface tension [35,36]. Thus, a wider melt pool was measured at higher laser powers. The largest width (163–176 μm) was attributed to the single tracks with a laser power of 150 W, whereas the smallest width (58–81 μm) was measured at a laser power of 50 W.

Fig. 5(a)-(b) presents the average depth of the melt pool as a function of laser power and wt% NP and NC, respectively. Similar to the track width, the melt pool depth showed a linear relationship with laser power; higher laser power led to a deeper melt pool. The depth of the melt pool was controlled by conduction [37]. To form a good bonding between the powder and the build plate, the liquid must have sufficient enthalpy to melt both the powder and the underlying solid material. This is why melt pool depth increased by increasing the laser power from 50 to 150 W (more heat per unit time in a unit length was achieved).

Furthermore, melt pool depth increased by adding second phase reinforcement of Al_2O_3 NPs or Al_{13} NCs to 316L powder. The addition of Al_2O_3 NPs showed a deeper melt pool in comparison to the 316L. For example, at a laser power of 150 W, the melt pool depth of 316L and 316L+ 5 wt% Al_2O_3 NPs were 213 ± 7 μm and 249 ± 11 μm, respectively. These deeper melt pools in nanocomposites single tracks can be attributed to the role of the second phase (Al_2O_3 NPs) in enhancing the laser energy absorption because of higher surface roughness caused by the second phase particles as formerly shown in the inset of Fig. 1(b)-(c). Fluid flow in the melt pool is mainly controlled by thermo-capillary force and viscous drag [38]. The addition of NPs on the surface of metal powder could intensify the number of reflections inside the powder bed and improve the laser absorptivity of metal power thus intensifying the heat input [39]. Additionally, the presence of Al_2O_3 NPs

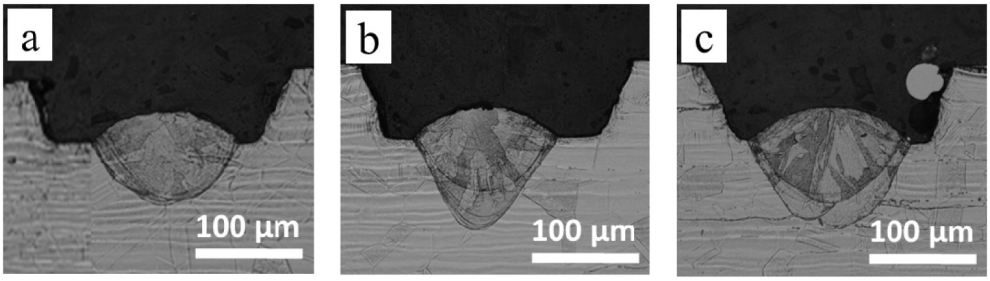

Fig. 3. Cross-section of deposited single tracks at 100 W with (a) 316L, (b) 316 + 1 wt% Al_2O_3 NPs, and (c) 316 + 1 wt% Al_{13} NCs.

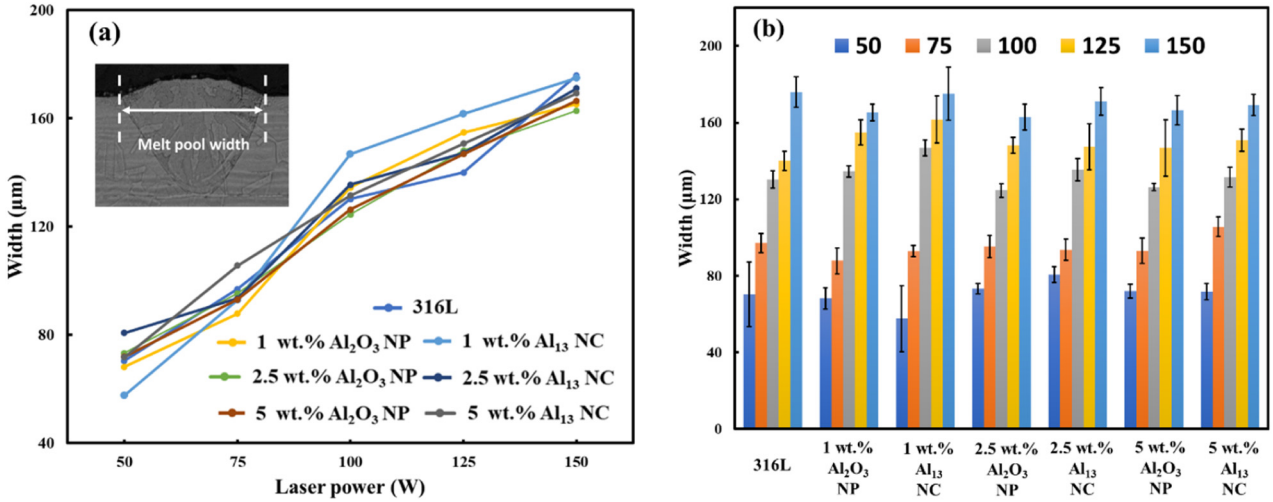

Fig. 4. Average melt pool width of deposited single track as a function of (a) laser power, and (b) wt% of NPs/NCs.

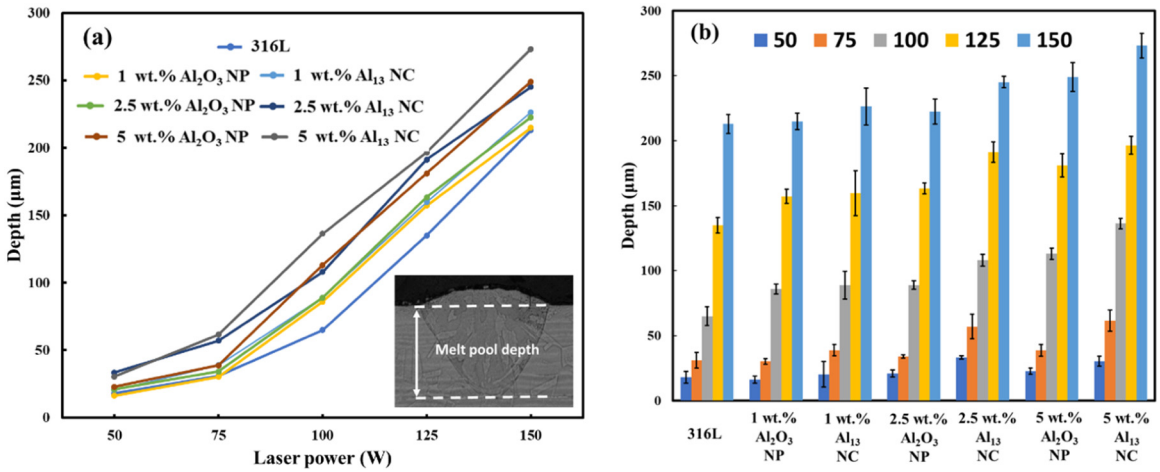

Fig. 5. Average melt pool depth of deposited single tracks as a function of (a) laser power, and (b) wt% of NPs/NCs.

could decrease the effective thermal conductivity of the 316L matrix by introducing an interfacial thermal resistance and scattering the energy carriers (electrons and photons) that would conduct the heat [39]. Reduced thermal conductivity could prevent efficient heat transfer to the bulk material (build plate) and intensify heat accumulation within the melt pool. In addition, NPs significantly increased the viscosity and thereby suppressed the thermo-capillary flow and hindered the effective heat transfer within the melt pool [21]. Therefore, it could be concluded that the combined effect of reinforcements addition, enhanced laser absorptivity, retarded heat dissipation, and increased viscosity could lead to a deeper melt pool.

At the same laser power, the Al_{13} NCs deposited single tracks revealed deeper melt pools compared to Al_2O_3 NPs. For example, at a laser power of 150 W, the melt pool depth of 316L + 2.5 wt% Al_2O_3 NPs and 316L+ 2.5 wt% Al_{13} NCs were 223 ± 10 μm and 245 ± 4 μm, respectively. Deeper melt pools in Al_{13} NCs samples could be explained by the fact that the Al_{13} NCs precipitated a very fine nanocluster of Al_{13} (<2 nm in size) upon evaporation of ethanol [30], comparatively finer than Al_2O_3 NPs (20 nm in size). Smaller NCs result in more scattering on the laser energy and larger thermal resistance interfacial area [40]; Therefore, a deeper melt pool was achieved in 316L/Al_{13} NCs samples in comparison with 316L/Al_2O_3 NPs. Additionally, because Al_{13} NCs had a smaller particle size than Al_2O_3 NPs, the effective viscosity was further reduced [41] and resulted in a deeper melt pool in the case of 316L/Al_{13} NCs composite.

Fig. 6(a)-(c) shows the formation of voids at the deposited single tracks at 150 W for 316L, 316 + 5 wt% Al_2O_3 NPs, and 316 + 5 wt% Al_{13} NCs, respectively. In the deposited single track of 316L (Fig. 6a), a very small pore with the size of ~8 μm was formed at the bottom of the melt pool. However, much larger pores (~25 μm) were formed at the melt pools of 316L + 5 wt% Al_2O_3 NPs and 316L + 5 wt% Al_{13} NCs as shown in Fig. 6(b)-(c). According to King et al. [37], the conduction mode is identified when the melt pool depth is lower than its width and forms a semi-circular shape. However, if the laser VED exceeds certain criteria, a transformation from conduction mode to keyhole mode occurs [42]. The criteria of keyhole mode are when the depth of the melt pool becomes greater than half the width of the melt pool. In keyhole mode, the laser power is high to evaporate the metal; forming plasma. Metal evaporation consequently causes a recoil pressure and a vapor cavity that further enhances the laser absorption and the laser beam drill to a deeper depth than that of the conduction mode. Finally, the walls of the cavity collapse and leave behind pores at the deepest point of melt pools, as shown in Fig. 6(b)-(c). In this study, NPs and NCs effectively reduced thermal conductivity in the 316L matrix and led to the formation of larger pores due to a pronounced keyhole mode.

To study the effect of the addition of NPs and NCs on the mode of welding, Supplementary Fig. 5 shows the depth/half-width ratio of the melt pools for 316L, 316L+(1, 2.5, 5) wt% Al_2O_3 NPs, and 316L+(1, 2.5, 5) wt% Al_{13} NCs at different laser powers ranging from 50 to 150 W. At

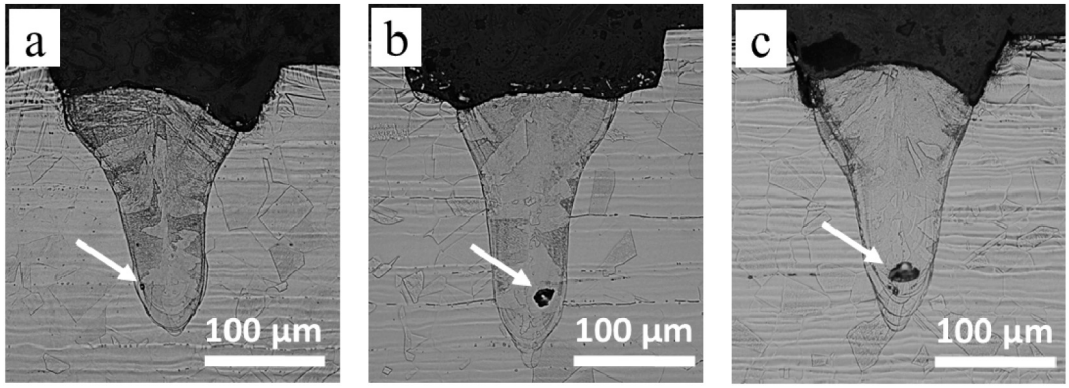

Fig. 6. Cross-section of deposited single tracks at a laser power of 150 W and a scan speed of 200 mm/s with (a) 316L, (b) 316 + 5 wt% Al_2O_3 NPs, and (c) 316 + 5 wt% Al_{13} NCs (arrows are showing gas pores at the bottom of the melt pools formed due to cavity walls collapsing).

every laser power, the addition of NPs and NCs changed the depth/half-width ratio of single tracks, mainly due to the change in the depth of each melt pool. For example, at 100 W, the deposited single track of 316L demonstrated a depth/half-width ratio of 0.99 which was attributed to the conduction mode. However, by the addition of 1 wt% of Al_2O_3 NPs and Al_{13} NCs the depth/half-width ratio was raised to 1.28 and 1.20, respectively, attributed to keyhole mode. By increasing the laser power to 125 W and 150 W in 316L single track, the depth/half-width ratio, increased to 1.92 and 2.44, respectively; implying an abrupt change in the mode of welding.

3.2. Top surface morphology of single-tracks

SEM micrographs in Fig. 7(a)-(o) present the top surface morphology of multiple deposited tracks at laser powers of 50, 100, and 150 W. The deposited 316L single track at 50 W showed a semi-continuous track was formed. The zone around the track became heavily populated with satellites and droplets that were spattered due to the Plateau-Rayleigh instability [43,44]. A continuous 316L single track was formed at a laser power of 100 W. Laser power higher than 100 W did not show a significant change in the morphology of the top surface of the melt track.

At laser power of 50 W, the addition of 1 wt% Al_2O_3 NPs led to a uniform track compared to the 316L track at the same power, as shown in Fig. 7(d). This is because NPs added to melt significantly increased the viscosity of the melt track; reducing the number of satellites. Ma et al. [21] reported similar results on adding NPs of SiC to Ni matrix that reduced surface asperities. By increasing the amount of Al_2O_3 NPs to 5 wt% at a laser power of 50 W, the number of satellites was significantly

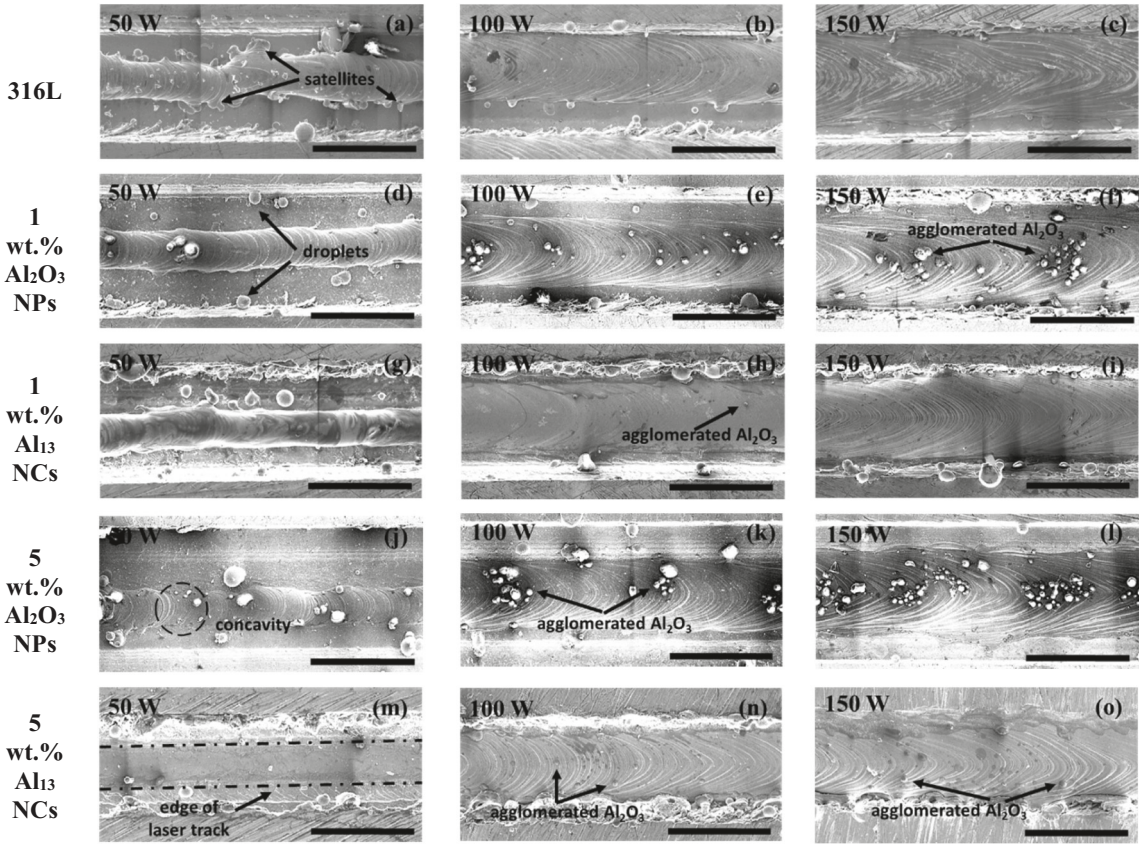

Fig. 7. SEM micrographs showing the morphology of the top surface of multiple single tracks at a laser power of 50, 100, and 150 W (the scale bar is 200 µm).

reduced and as shown in Fig. 7(j), a concavity has been observed on the top surface of the single track; implying an instability happened in the deposited single track at higher wt% of NPs.

At 50 W, adding 5 wt% Al_{13} NCs to 316L made the track almost invisible because the entire length of the track was depressed to the build plate, as the edges of the track were annotated in Fig. 7(m). The measured height and depth of this track were 3 ± 1 μm and 30 ± 4 μm, respectively. The extremely low bead height could be explained by lower thermal conductivity of the melt pool after the addition of reinforcements; the accumulation of heat in the melt pool resulted in the depression of the melt pool to the build plate.

The EDS analysis shown in Supplementary Fig. 6 confirmed that large white particles formed on the top surfaces of deposited nanocomposites single tracks in Fig. 7 were mainly aluminum oxide. In the case of the addition of Al_2O_3 NPs to the 316L single track, it is possible that during melting, the NPs agglomerated together and formed particles, ranging from 5 to 40 μm, which was substantially greater than the initially added NPs (size: ~20 nm) and eventually these agglomerated particles floated to the top surface. The density of these particles can be considered as the density of Al_2O_3 (3.95 g/cm^3) which is half of the

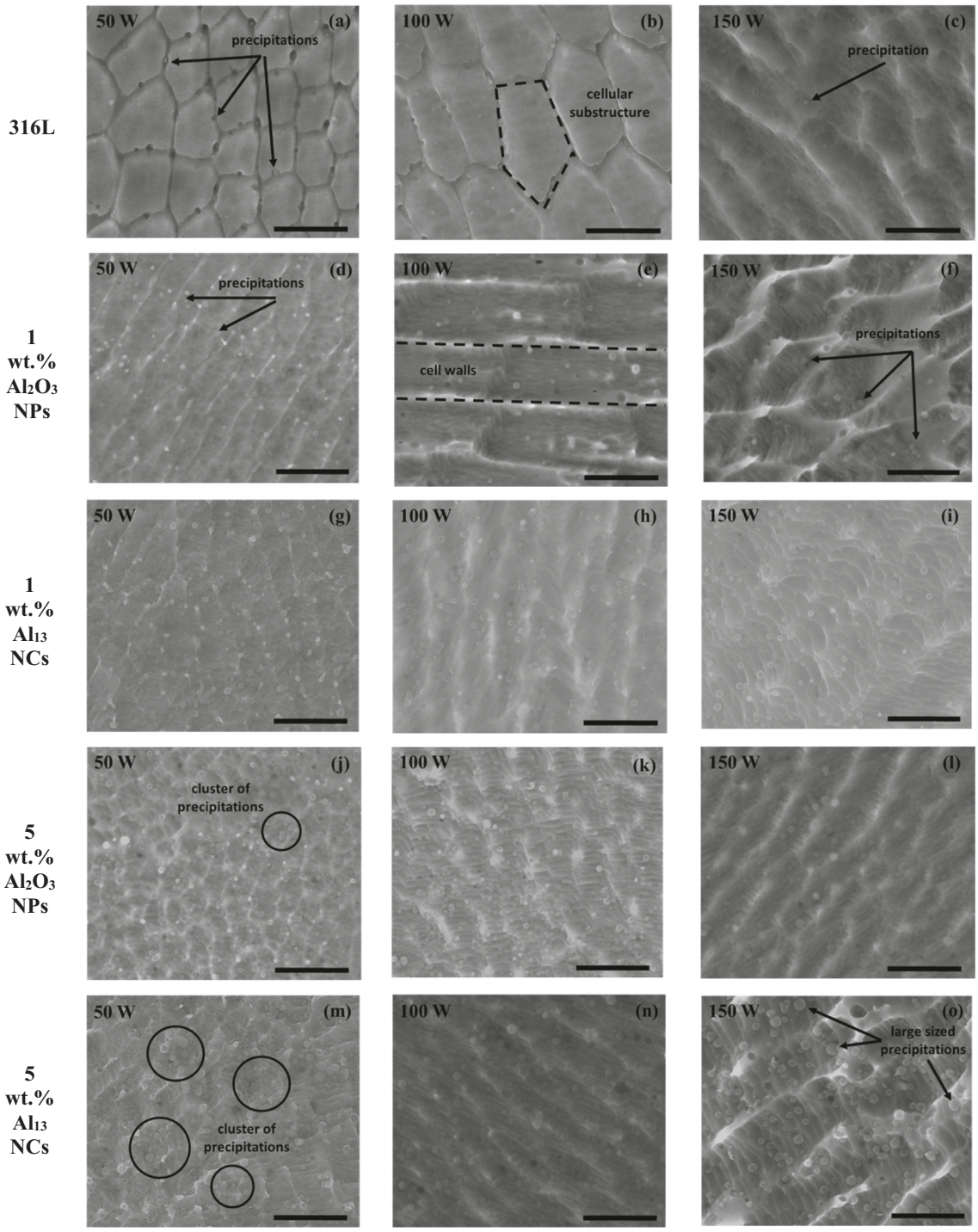

Fig. 8. SEM micrographs of the cross-section of single tracks of 316L with various additions of second phase reinforcement at laser powers of 50, 100, and 150 W (scale bar is 1 μm in all the micrographs).

density of 316L SS (8 g/cm^3); causing a significant buoyancy force and pushing these particles to the top surface of the deposited tracks.

As can be observed from Fig. 7(d)-(f), in the deposited single track with 1 wt% Al_2O_3 NPs, by increasing the laser power from 50 to 150 W, the number of agglomerated particles on the surface increased, however, the size of them were smaller at a higher laser power of 150 W compared to 50 W. Increasing the laser power from 50 W to 150 W intensified the Marangoni convection flow and led to pronounced stirring and turbulence in the melt pool which indeed distributed nanoparticles into smaller agglomerated particles. The fraction of agglomerated particles was increased with a further increase in wt% of Al_2O_3 NPs due to the matrix solubility limit. These agglomerated particles could get coarsened during the LPBF process and subsequently disturb the powder spreadability in the next layers [45]. The formation of similar agglomerated oxide particles in producing bulk MMNCs is reported in Ref. [10,46].

The agglomeration of Al_2O_3 particles on the surface was mitigated when Al_{13} NCs were added onto the 316L matrix. As shown in Fig. 7(h), (i), and (n), the amount and size of agglomeration in Al_{13} NCs samples were drastically lower than 316L/Al_2O_3 nanocomposite samples which implied that the in-situ conversion of nanoparticles could drastically reduce their agglomeration.

3.3. Microstructure characterization of the deposited single-track nanocomposites

Fig. 8(a)-(o) shows the microstructure of the deposited 316L, 316L/Al_2O_3 NPs, and 316L/Al_{13} NCs single tracks at laser powers of 50, 100, and 150 W, respectively. An LPBF-typical austenitic cellular substructure (~1 μm) was formed in the deposited single tracks due to a high cooling rate [47,48]. It can be observed from Fig. 8 that there were some precipitations in all of the deposited single tracks, however, the size and number density of these precipitations varied through different samples. In 316L deposited single track, the number density of precipitations was very low, as annotated in Fig. 8(a) and by increasing the laser power from 50 to 150 W, just a very few precipitations were detected in the matrix, Fig. 8(c). As previously reported by Saeidi et al [49] in the LPBF process of 316L, these precipitations were silicate and enriched in Si, Mn, and O. These silicate precipitations were formed due to the high oxygen affinity of Si and Mn, compared to other alloying elements inside the 316L composition and is kinetically favored during the process of laser melting of 316L [49]. These precipitations mainly formed at the cell boundaries as annotated in Fig. 8(a), rather than inside the cell.

The matrix of deposited single tracks of 316L/Al_2O_3 NPs and 316L/Al_{13} NCs nanocomposites as illustrated in Fig. 8, showed a large number of precipitations with different sizes varying through all the samples. These precipitations were distributed uniformly in the matrix as shown in Fig. 8(d) and (g) without showing any clustering. However, by increasing the wt% of Al_2O_3 NPs and Al_{13} NCs in the 316L matrix to 5 wt %, clustering of precipitations was detected as annotated in Fig. 8(j) and (m). By increasing the laser power from 50 to 150 W, a very similar trend to 316L single track in reducing the number of precipitations can be detected, regardless of the amount of initially added NPs/NCs.

Fig. 9(a)-(b) shows the wt% fraction and average size of precipitations according to the measurement of different SEM micrographs from different cross-sections; counting at least 1000 precipitations; considering the density of precipitations was 3.95 g/cm^3 ($\rho_{Al_2O_3}$= 3.95 g/cm^3). For example, at 50 W, increasing the amount of Al_2O_3 NPs from 1 to 5 wt% in the deposited single track increased the wt% of precipitation from 3.87 to 6.3 wt% in the matrix, respectively, whereas deposited single tracks with Al_2O_3 NPs and Al_{13} NCs showed a slightly higher concentration (wt%) compared to the amount that was initially added to the precursor powder. This discrepancy in obtained concentration in terms of precipitated nanoparticles could be explained by different and contradicting factors such as agglomeration of Al_2O_3 particles and floating to the top surface, and formation of complex Al-Si-O-enriched precipitation in the matrix, as will be discussed in the next section, instead of pure Al_2O_3 precipitation.

Fig. 9(a) shows that by increasing the laser power from 50 to 150 W the fraction of precipitations (wt%) in all samples was reduced. This decrease in the precipitation wt% of 316L/Al_2O_3 NPs can be attributed to the role of higher laser power which increased the temperature and Marangoni flow in the melt pool; providing sufficient time for agglomeration of Al_2O_3 NPs and floating to the top surface of the melt pool, as previously shown in Fig. 7 where laser power of 150 W showed more agglomeration of Al_3O_2 particles on the surface as compared to 50 W deposited single tracks.

Overall, the fraction of precipitations in the 316L/Al_{13} NCs was higher than 316L/Al_2O_3 NPs implying a higher fraction of reinforcement particles were added in the form of NCs. For example, the fraction of precipitations in 5 wt% Al_{13} NCs was 2.58 wt% which was higher than the same value of 5 wt% Al_2O_3 NPs (1.99 wt%) at a laser power of 100 W. Furthermore, at higher laser power, the fraction of precipitations was observed to be significantly higher in 316L/Al_{13} NCs than in the same sample with Al_2O_3 NPs. For example, at 150 W, the sample with 5 wt% Al_{13} NCs showed 1.45 wt% of precipitations, and the sample produced with 5 wt% Al_2O_3 showed only 0.36 wt% of precipitations. According to micrographs from top surfaces (Fig. 7) and cross-sections (Fig. 8), it is plausible to conclude that Al_{13} NCs nanocomposites created less agglomeration than Al_2O_3 NPs at higher laser powers. Thus, the in-situ conversion of NCs as a result of doping the ink was more effective in homogenous dispersion of reinforcement particles than adding NPs through light mixing (ex-situ).

The precipitation size increased at higher laser power as shown in

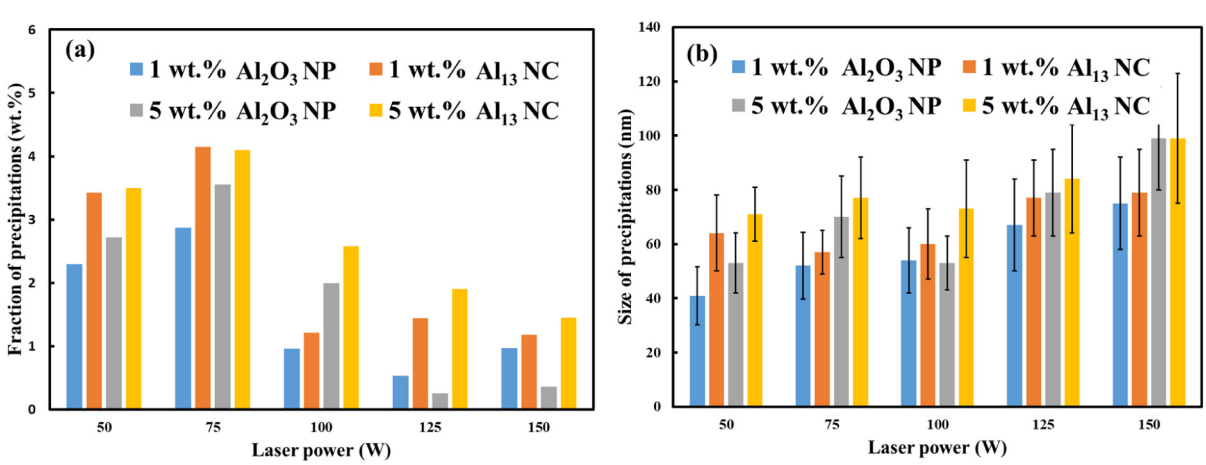

Fig. 9. (a) wt% of precipitations and (b) average size of precipitations in a deposited single track of 316L/Al_2O_3 NPs and 316L/Al_{13} NCs at laser powers of 50–150 W.

Figs. 8(o) and 9(b). For example, the size of precipitation in 316L + 1 wt % Al_2O_3 nanocomposite increased from 41 ± 11 nm at 50 W to 75 ± 17 nm at 150 W. This is because increasing the heat input increased the lifetime of liquid; providing ample time for diffusion of elements to the precipitates. Additionally, higher heat input induced more Marangoni flow that could accelerate the solute diffusion in the melt pool and facilitate precipitate coarsening. Furthermore, by increasing the wt% of NPs and NCs, the size of precipitation was slightly increased. For instance, at a laser power of 100 W, the size of precipitates increased from 60 ± 13 nm to 73 ± 18 nm associated with 1 and 5 wt% in Al_{13} NCs, respectively.

3.4. Detailed microstructure characterization

Fig. 10(a)-(b) shows the microstructure of 316L/1 wt% Al_2O_3 NPs and 316L/1 wt% Al_{13} NCs, respectively both manufactured at a laser power of 100 W. High dislocation density, as shown in the inset of Fig. 10(b), was observed in both samples due to the rapid solidification rate of the LPBF process. Using different STEM micrographs and adopting the line-intercept method, the average dislocation density was calculated to be 1.14×10^{14} (m^{-2}) and 1.32×10^{14} (m^{-2}) for 316L/1 wt % Al_2O_3 NPs and 316L/1 wt% Al_{13} NCs, respectively. According to Fig. 10(b), precipitations were distributed at the grain boundaries and in grains interior and the diameter of these precipitations ranged between 25–95 nm and 18–91 nm for 1 wt% Al_2O_3 NPs and 1 wt% Al_{13} NCs, respectively.

Fig. 11 shows a high angle annular dark-field (HAADF) STEM micrograph and corresponding EDS elemental map of 316L/1 wt% Al_2O_3 NPs deposited at a laser power of 100 W. The EDS elemental map revealed that the precipitates were enriched in Al, Si, Mn, and O.

As formerly shown in Fig. 1(b), the morphology of Al_2O_3 NPs remained unchanged after light mixing of 316L and Al_2O_3 powder, and Al_2O_3 NPs did not dissolve into the 316L powder matrix. However, after deposition of single-track nanocomposites the morphology and composition of nanoparticles transformed, conveying that the Al_2O_3 NPs were partially melted during the laser process and precipitated as Al-enriched precipitations. This phenomenon can be explained by the fact that the distribution of Al_2O_3 NPs on the surface of 316L metal powder after light mixing directly expose them to the laser beam (50 μm) which was much larger than Al_2O_3 NPs size (20 nm). The laser energy is absorbed on the surface of any 316L particles, producing a high temperature on the surface of the metal powder particle during the interaction. The high surface-to-volume ratio of NPs (size = 20 nm) combined with the fact the high temperature on the surface powder could reach the boiling point of the metal powder [50] cause the Al_2O_3 NPs to partially melted during the interaction with the laser. Dissolved Al and O atoms would react with the available Si (0.64 wt%) and Mn (0.74 wt%) being pushed away from the 316L liquid during solidification and formed Al-Mn-Si-O-enriched precipitations. The Gibbs free energy for the formation of Al_2O_3, SiO_2, and MnO are the lowest among the other elements in 316L [51] as listed in Table 2. Thus, the formation of Al-Si-Mn-O-enriched precipitations is likely due to the reaction of dissolved Al, Si, and Mn with dissolved O atoms or any residual O available in the LPBF chamber (O < 100 ppm).

Fig. 12 shows the EDS elemental map of 316L/1 wt% Al_{13} NCs and precipitation of Al-enriched nanoparticles very similar to precipitated nanoparticles in a deposited single track of 316L/1 wt% Al_2O_3 NPs. The Al_{13} NCs, according to the reaction Eq. (1), can provide the necessary Al atoms in the melt pool and form a supersaturated solid solution. The Al has limited solubility in the austenite phase therefore, the Al atoms could react with available Si, Mn, and O in the melt pool and form Al-Mn-Si-O-enriched precipitations in deposited single track 316L/1 wt% Al_2O_3 NPs.

3.5. Role of NPs/NCs in grain size of the deposited single-tracks

Fig. 13(a)-(c) shows the EBSD IPF maps analysis performed on the cross-section of single tracks deposited at 100 W for 316L, 316L/1 wt% Al_2O_3 NPs and 316L/1 wt% Al_{13} NCs, respectively. The columnar grains elongated along the fusion line and aligned in the direction of the thermal gradient (epitaxial growth) were observed in Fig. 13(a)-(c) [34]. Fig. 13(d) illustrates that the columnar grain size in deposited nanocomposite tracks was larger than 316L deposited tracks. The average grain size of 316L, 316L/1 wt% Al_2O_3 NPs and 316L/1 wt% Al_{13} NCs were 7 ± 6.5 μm, 7.8 ± 8.7 μm and 10 ± 12.2 μm, respectively. The NPs and NCs increased the viscosity of the melt and reduced the thermal conductivity and solidification rate. Therefore, grain nuclei had a longer time to grow into the melt pool, in the direction of heat dissipation, and formed larger grains. Furthermore, the grains in the deposited 316L/Al_{13} NCs were larger than 316L/Al_2O_3 NPs. As discussed in Section 3.1, the Al_{13} NCs size (<2 nm) was substantially smaller than the NPs size (20 nm); therefore, they would be more effective in increasing the viscosity; decreasing thermal conductivity [21]; extending the liquid lifetime and providing enough time before solidification to form larger grains in 316L/Al_{13} NCs single tracks.

The misorientation angle charts presented in Fig. 13(e) demonstrated that the fraction of low angle grain boundaries (LAGBs) with misorientation of <10° were 0.7, 0.5, and 0.6 for 316L, 316L/1 wt% Al_2O_3, and 316L/1 wt% Al_{13} NCs, respectively. This relatively high fraction of LAGBs was attributed to the high dislocation density induced by high thermal stresses. The addition of NPs and NCs had a minor effect on the fraction of LAGBs in single tracks.

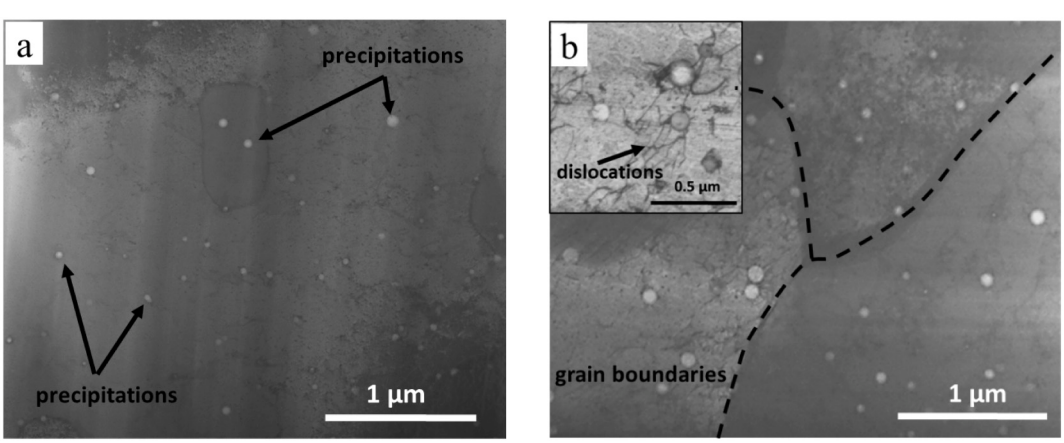

Fig. 10. Bright-field STEM micrograph of (a) 316L/1 wt% Al_2O_3 NPs (b) 316L/1 wt% Al_{13} NCs single tracks deposited at laser power of 100 W.

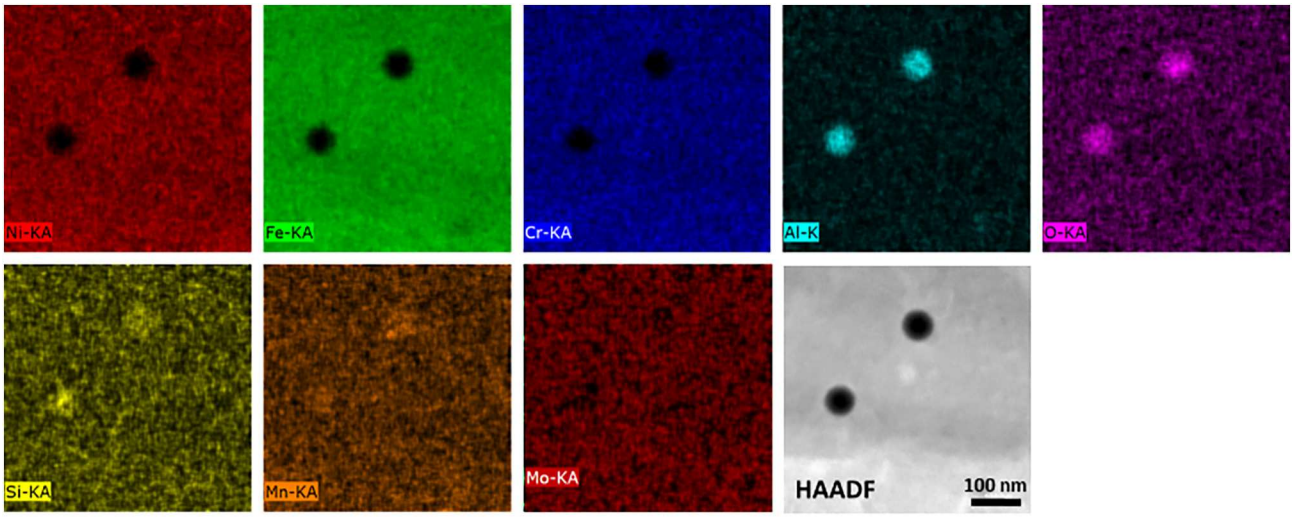

Fig. 11. HAADF STEM micrograph with corresponding EDS elemental map obtained from precipitations of 316L/1 wt% Al_2O_3 nanocomposite single track (laser power: 100 W).

Table 2
The equilibrium partial pressure of oxygen and Gibbs free energy for the formation of various oxide compound at 1400 °C [51].

Element	Stoichiometric composition	P_{O2} (atm)	Gibbs free energy, ΔG ($kJ \cdot mol^{-1}$)
Fe	Fe_3O_4	7.29×10^{-10}	−292.9
	Fe_2O_3	6.02×10^{-9}	−263.5
Cr	Cr_2O_3	3.15×10^{-15}	−464.6
Ni	NiO	1.90×10^{-6}	−183.6
Mo	MoO_2	4.15×10^{-10}	−299.9
Si	SiO_2	7.10×10^{-20}	−612.5
Mn	MnO	8.10×10^{-18}	−546.9
Al	Al_2O_3	1.61×10^{-24}	−760.7

3.6. Microhardness analysis

Fig. 14(a)-(b) shows the microhardness measurements for different single tracks as a function of laser power and wt% of Al_2O_3 NPs/Al_{13} NCs, respectively. The microhardness of the annealed 316L was 160 HV [52]. The average microhardness value of the 316L single track deposited at the different laser powers (50–150 W) was 265 ± 15 HV, and this increase compared to the annealed condition could be attributed to the high dislocation density and finer grains size induced by rapid melting and solidification [34]. By the addition of 1 wt% Al_2O_3 NPs to the 316L matrix, the hardness of the deposited single track increased by 7 % and reached the average of 285 ± 13 HV. A similar trend can be observed in 316L/1 wt% Al_{13} NCs deposited single track and the microhardness increased by ~10 %, 293 ± 7 HV. In 316L/1 wt% Al_2O_3 NPs and 316L/1 wt% Al_{13} NCs samples, there was some fluctuation in the microhardness values at different laser powers.

At the high laser power of 150 W, by increasing the wt% of reinforcement phase to 2.5 and 5 wt%, the microhardness drastically dropped to the values below the deposited 316L single track. For example, the microhardness of 316L/5 wt% Al_2O_3 NPs was 219 ± 14 HV which was the lowest microhardness measured in this study. According

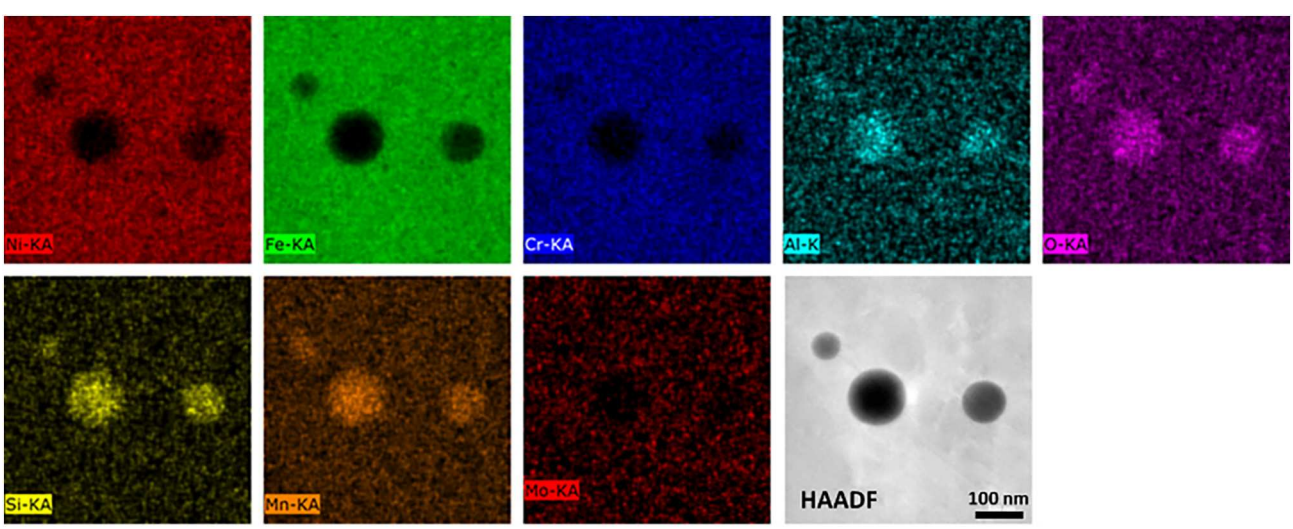

Fig. 12. HAADF STEM micrograph with corresponding EDS elemental map obtained from precipitations of 316L/1 wt% Al_{13} NCs nanocomposite single track (laser power: 100 W).

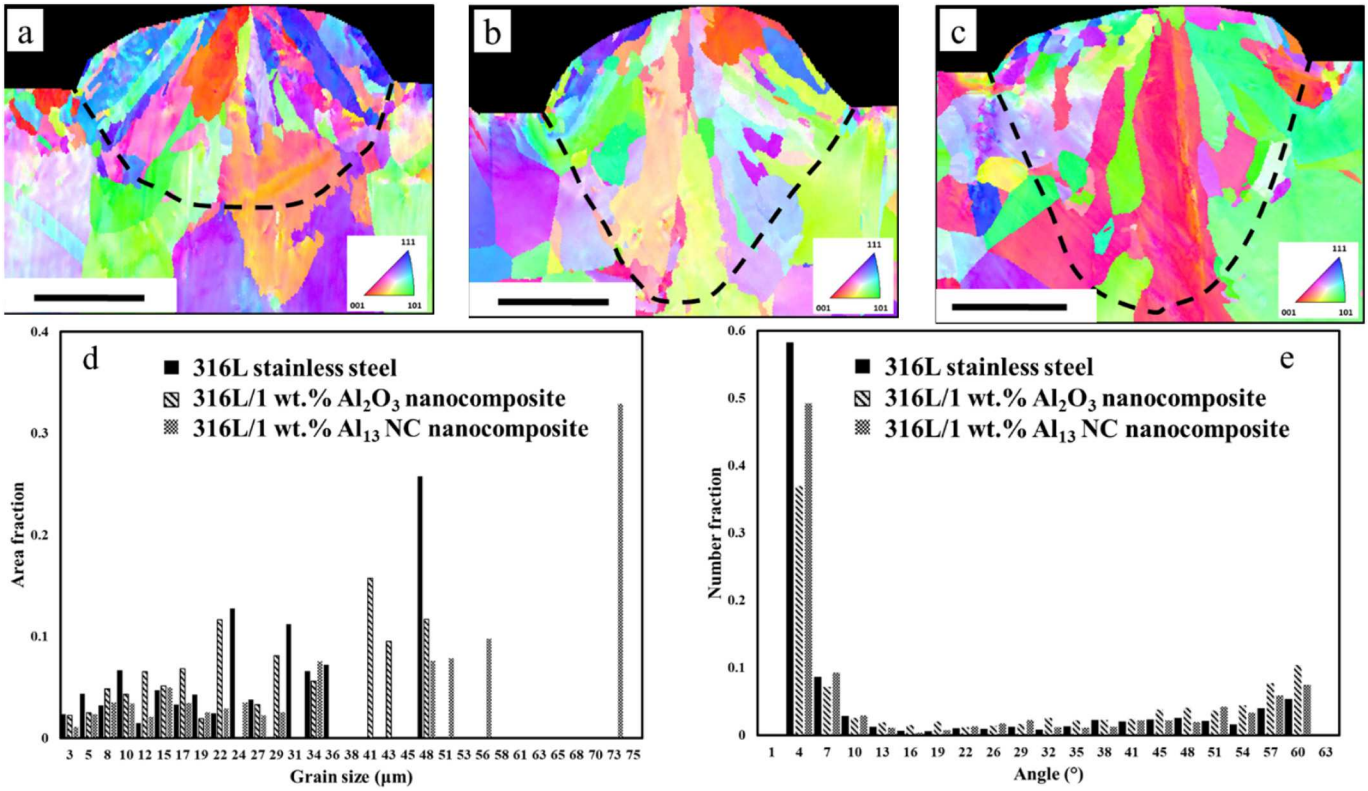

Fig. 13. EBSD IPF maps of deposited single tracks (a) 316L, (b) 316L/1 wt% Al_2O_3 NPs, (c) 316L/1 wt% Al_{13} NCs (d) grain size distribution of deposited tracks, and (e) misorientation angle distribution (the scale bar is 50 μm).

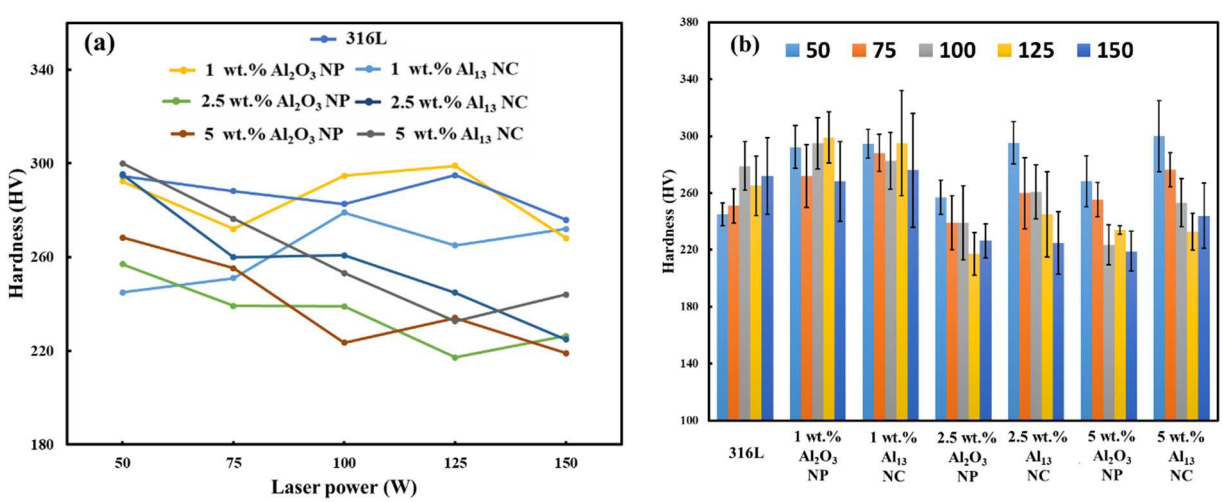

Fig. 14. Microhardness measurement of deposited single track as a function of (a) laser power and (b) wt% of Al_2O_3 NPs/Al_{13} NCs.

to the Ashby-Orowan relationship, the strength of a material is directly related to the fraction of precipitations that can be expressed as:

$$\Delta H_{Or} \approx \sqrt{f} \tag{2}$$

where ΔH_{Or} represents the precipitation strengthening increment and f is the precipitate volume fraction. Therefore, and as previously shown in Fig. 9(a), the wt% fraction of precipitations drastically reduced in the case of the addition of 5 wt% NPs/NCs, resulting in reduced hardness values, especially at higher laser powers in which higher agglomerated Al_2O_3 particles were observed on the surface of tracks, Fig. 7.

In addition to the reduction in the fraction of precipitation, the decrease in hardness at higher laser power can also be attributed to the formation of larger grains at higher VED. The higher laser power led to grain growth [34] and reduced the hardness according to Eq. (3). A similar trend has been reported by AlMangour et al. [53] in producing LPBF 316L/TiC nanocomposites and the hardness values dropped by ~25 % by utilizing a higher VED.

$$\Delta H_{Hall-Petch} \approx 1/\sqrt{d} \tag{3}$$

In general, adopting the Al_{13} NCs led to greater hardness values in comparison to Al_2O_3 NPs, and this largely could be explained by the higher fraction of precipitations in the deposited single tracks of nanocomposites. Therefore, it can be concluded that adopting an in-situ method for producing nanocomposites is a promising approach to

achieving a higher fraction of precipitations in the MMCs.

4. Hybrid LPBF+Ink-jetting tool

In order to show the feasibility of producing the 316L/Al_2O_3 nanocomposite using our novel proposed method and also the ability to selectively adjust the properties through the build, three cylinders with the dimension of D8 × 8 mm has been printed; utilizing the hybrid LPBF+ink-jetting tool that has been modified at Oregon State University. Further details about the modification of this hybrid printer and producing coupons can be found in Supplementary and elsewhere [54]. This tool enables us to selectively add ink to certain layers to tailor properties. In our single-track experiment, the addition of Al_{13} NCs ink to the 316L matrix showed that the microhardness of a sample could be improved very similar to the addition of Al_2O_3 NPs to the 316L matrix, however, this novel hybrid approach as demonstrated here, enables us to move one step forward in tailoring properties of a printed part adopting LPBF process and assign a specific property, in our case improved microhardness, to defined layers.

Fig. 15 shows the printed coupon and the schematic of the order of zones for printing 316L powder and zones with the jetting of Al_{13} NCs ink. The detailed sequences of manufacturing these zones within the coupons can be found in the Supplementary section and Supplementary videos 1-3. To check the practicality of our approach to enhancing the mechanical properties, the microhardness test was conducted on the printed sample by averaging 10 data points within the same zone. The average microhardness values of 316L and 316L/Al_{13} NCs zones were 240 ± 22 HV and 274 ± 17 HV, respectively. As expected from the single-track experiment, the addition of Al_{13} NCs ink to the 316L matrix enhanced the microhardness of nanocomposite zones by ~10–15 %. This measurement demonstrates that by selectively adding Al_{13} NCs ink to predefined layers, the mechanical properties of particular zones can be enhanced.

Fig. 16 shows the microstructure of two zones with different characteristics, one zone was printed with 316L SS powder (Fig. 16(a)), and the other zone was printed with 316L/Al_{13} NCs (Fig. 16(b)). Similar to the microstructure of previously shown in deposited 316L/Al_{13} NCs single-track, in the zone in which Al_{13} NCs ink has been jetted, the microstructure consists of the Al-enriched precipitations, as previously shown in Fig. 12. On the other side, the printed 316L zones showed a meniscal amount of precipitations which was in agreement with single-track experiment of 316L powder.

This study was intended to present a novel hybrid approach to produce nanocomposites that enables us to selectively add specific properties to certain layers, in our case, improving the hardness. In the future, the investigation will be focused on controlling the solid loading of the ink and defining the important parameters to adjust the solid loading. In-situ jetting reinforcement nanoparticles to powder bed through a selective approach and dispersing particles in the melt pool via Marangoni flow will eliminate the need for ball-milling while delivering targeted properties. LPBF for manufacturing of MMCs is currently limited to ball-milling feedstock with the second-phase particles prior to spreading the layer of powder into the LPBF chamber. The contribution of this work will be significant because it is expected to revolutionize the use of LPBF as a means of in-situ variation of the composition, achieving targeted properties and eliminating the need for ball-milling. The outcome will be simplifying the manufacturing steps, reducing time and cost and meanwhile, and distributing nanoparticles via a selective approach. This is expected to have significant positive impacts in the areas of selective doping, additive manufacturing of MMCs and FGAs with targeted properties, and reduced cost and time.

5. Conclusions

The LPBF process has been widely adopted in the manufacturing of MMNCs and ball milling is the main method of producing the feedstock. Ball milling, inherently, is a very time-consuming process that is not cost-effective, and ball-milling cannot create a voxel-controlled composition and properties during LPBF. In this work, a new method is demonstrated to manufacture MMNCs through hybrid AM of LPBF coupled with mature ink-jetting technology. To understand the fundamental knowledge gap on the effect of adding second phase reinforcement nanoparticles to the melt pool, and identify the mechanism(s) for selectively adding and dispersing nanoparticles via Marangoni flow a single track was manufactured via a hybrid LPBF+ink-jetting process. Two approaches were compared here; Al_2O_3 NPs were mixed with 316L using light milling and then a single track was deposited, and Al_{13} NCs were jetted onto a layer of 316L (no milling) before laser melting and converted to Al_2O_3 during LPBF. The main conclusions can be drawn as follows:

1. The addition of Al_2O_3 NPs and Al_{13} NCs to 316L single tracks significantly increased the depth of the melt pool. Because NPs/NCs decreased the thermal conductivity and increased the viscosity; preventing efficient heat transfer to bulk material (build plate). Due to the finer size of Al_{13} NCs compared to Al_2O_3 NPs, the 316L/Al_{13} NCs deposited single track showed deeper melt pools, comparatively.
2. In both 316L/Al_2O_3 NPs and 316L/Al_{13} NCs nanocomposites, Al-enriched precipitations were detected in the 316L matrix. The high energy of the laser melts Al_2O_3 NPs and converts Al_{13}; providing Al atoms in the melt pool. Due to the lower Gibbs free energy of

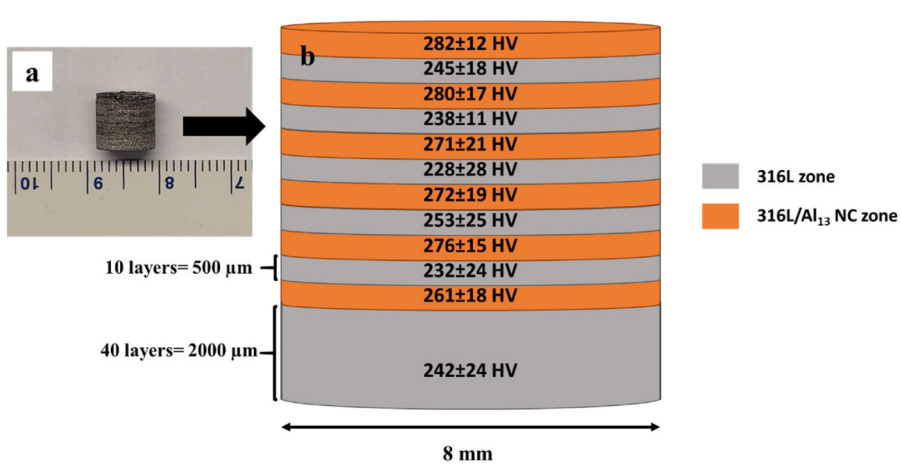

Fig. 15. (a) Manufactured cylinder adopting the Hybrid LPBF+Ink jetting printer with alternation zones, 316L zone, and 316L/Al_{13} NCs zone, (b) schematic of different zones in the printed cylinder; microhardness values of each zone were reported.

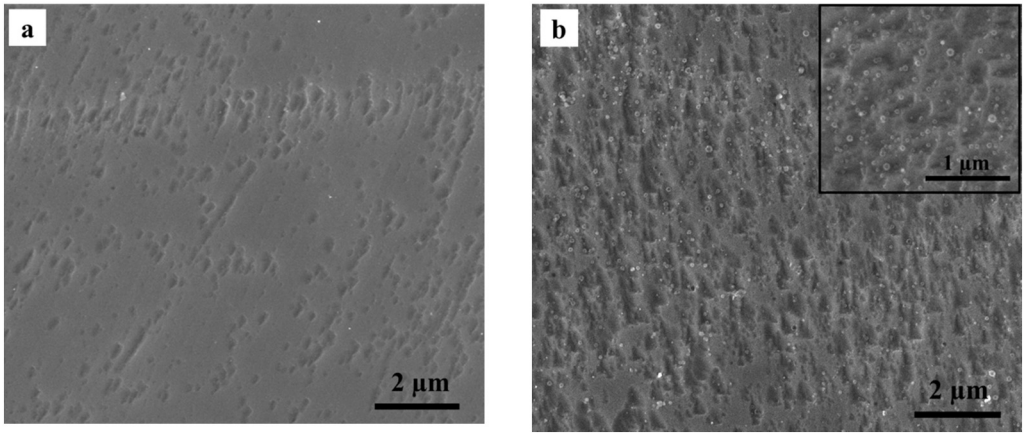

Fig. 16. SEM micrograph of (a) 316L zone and (b) 316L nanocomposite zone; precipitations of Al-enriched particles can be observed in the 316L matrix (inset).

formation of Al, Si, and Mn; the Al-enriched precipitations formed in the matrix.

3. EBSD analyses confirmed that the addition of Al_2O_3 NPs and Al_{13} NCs increased the viscosity of the melt and prevented efficient heat transfer to the bulk material. Therefore, increasing the lifetime of the melt resulted in the formation of larger grains, specifically in 316L/Al_{13} NCs in which the Al_{13} NCs were more effective in reducing the thermal conductivity.
4. The microhardness of 316L/1 wt% Al_{13} NCs nanocomposites were 293 ± 7 HV, about 10 % higher than deposited 316L single track (265 ± 15 HV) and this increase was attributed to the higher precipitation of Al-enriched nanoparticles.
5. Overall, hybrid LPBF+ink-jetting was a promising alternative approach to manufacturing MMCs such as oxide dispersion strengthened (ODS) alloys and will be further utilized in to manufacture FGAs. The hybrid LPBF+ink-jetting approach demonstrated that the microhardness of a printed part could be tailored selectively through the build by doping Al_{13} NCs ink to the 316L matrix.

Supplementary data to this article can be found online at https://doi.org/10.1016/j.jmapro.2023.01.059.

Declaration of competing interest

The authors declare that they have no known competing financial interests or personal relationships that could have appeared to influence the work reported in this paper.

Acknowledgments

The authors gratefully acknowledge the financial support of the National Science Foundation Advanced Manufacturing Program through Award Number 1856412. Any findings and conclusions are those of the authors and do not necessarily reflect the views of the National Science Foundation. The authors would also like to acknowledge the funding of critical equipment provided by the Murdock Charitable Trust (contract number: 2016231:MNL:5/18/2017), the RAPID Institute, Prof. Brian K Paul, and the U.S. DOE (contract number: DE-EE0007888). MG and SP thank Dr. Peter Eschbach at OSU electron microscopy center, ATAMI staff especially Nick Wannenmacher, Tom Winslow at WinTech Design, Dr. Mehran Amiri, and undergraduate researcher Miss. Gabrielle E. Paul.

References

[1] González C, Vilatela J, Molina-Aldareguía J, Lopes C, LLorca J. Structural composites for multifunctional applications: current challenges and future trends. Prog Mater Sci 2017;89:194–251.
[2] Casati R, Vedani M. Metal matrix composites reinforced by nano-particles—a review. Metals 2014;4(1):65–83.
[3] Wei Y, Chen G, Li M, Li W, Zhou Y, Xu J, Zhou W. High-precision laser powder bed fusion of 18Ni300 maraging steel and its SiC reinforcement composite materials. J Manuf Process 2022;84:750–63.
[4] Kang Y-C, Chan SL-I. Tensile properties of nanometric Al2O3 particulate-reinforced aluminum matrix composites. Mater Chem Phys 2004;85(2–3):438–43.
[5] Sharifi EM, Karimzadeh F, Enayati M. Fabrication and evaluation of mechanical and tribological properties of boron carbide reinforced aluminum matrix nanocomposites. Mater Des 2011;32(6):3263–71.
[6] Saheb N, Iqbal Z, Khalil A, Hakeem AS, Al Aqeeli N, Laoui T, Al-Qutub A, Kirchner R. Spark plasma sintering of metals and metal matrix nanocomposites: a review. J Nanomater 2012;2012.
[7] Hsu C, Chang C, Kao P, Ho N, Chang C. Al–Al3Ti nanocomposites produced in situ by friction stir processing. Acta Mater 2006;54(19):5241–9.
[8] Suryanarayana C, Al-Aqeeli N. Mechanically alloyed nanocomposites. Prog Mater Sci 2013;58(4):383–502.
[9] Mirzababaei S, Ghayoor M, Doyle RP, Pasebani S. In-situ manufacturing of ODS FeCrAlY alloy via laser powder bed fusion. Mater Lett 2021;284.
[10] Walker JC, Berggreen KM, Jones AR, Sutcliffe CJ. Fabrication of fe-cr-Al oxide dispersion strengthened PM2000 alloy using selective laser melting. Adv Eng Mater 2009;11(7):541–6.
[11] Cooke S, Ahmadi K, Willerth S, Herring R. Metal additive manufacturing: technology, metallurgy and modelling. J Manuf Process 2020;57:978–1003.
[12] Narasimharaju SR, Zeng W, See TL, Zhu Z, Scott P, Jiang X, Lou S. A comprehensive review on laser powder bed fusion of steels: processing, microstructure, defects and control methods, mechanical properties, current challenges and future trends. J Manuf Process 2022;75:375–414.
[13] Yan D, Ghayoor M, Coldsnow K, Pirgazi H, Poorganji B, Ertorer O, Tan K-S, Burns J, Isgor OB, Pasebani S. Laser powder bed fusion and post processing of alloy 22. Addit Manuf 2022;50:102490.
[14] Yadroitsev I, Gusarov A, Yadroitsava I, Smurov I. Single track formation in selective laser melting of metal powders. J Mater Process Technol 2010;210(12):1624–31.
[15] Pasebani S, Ghayoor M, Badwe S, Irrinki H, Atre SV. Effects of atomizing media and post processing on mechanical properties of 17–4 PH stainless steel manufactured via selective laser melting. Addit Manuf 2018;22:127–37.
[16] Yadroitsev I, Krakhmalev P, Yadroitsava I, Johansson S, Smurov I. Energy input effect on morphology and microstructure of selective laser melting single track from metallic powder. J Mater Process Technol 2013;213(4):606–13.
[17] Thijs L, Verhaeghe F, Craeghs T, Van Humbeeck J, Kruth J-P. A study of the microstructural evolution during selective laser melting of Ti–6Al–4V. Acta Mater 2010;58(9):3303–12.
[18] AlMangour B, Grzesiak D, Jenn M. Selective laser melting of TiC reinforced 316L stainless steel matrix nanocomposites: influence of starting TiC particle size and volume content. Mater Design 2016;104:141–51.
[19] AlMangour B, Grzesiak D, Yang J-M. Rapid fabrication of bulk-form TiB2/316L stainless steel nanocomposites with novel reinforcement architecture and improved performance by selective laser melting. J Alloys Compd 2016;680:480–93.
[20] AlMangour B, Grzesiak D, Yang J-M. Nanocrystalline TiC-reinforced H13 steel matrix nanocomposites fabricated by selective laser melting. Mater Des 2016;96:150–61.
[21] Ma C, Chen L, Cao C, Li X. Nanoparticle-induced unusual melting and solidification behaviours of metals. Nat Commun 2017;8:14178.
[22] Yu WH, Sing SL, Chua CK, Kuo CN, Tian XL. Particle-reinforced metal matrix nanocomposites fabricated by selective laser melting: a state of the art review. Prog Mater Sci 2019;104:330–79.
[23] Pasebani S, Dutt AK, Burns J, Charit I, Mishra RS. Oxide dispersion strengthened nickel based alloys via spark plasma sintering. Mater Sci Eng A 2015;630:155–69.
[24] Pasebani S, Charit I, Wu YQ, Butt D, Cole J. Mechanical alloying of lanthana-bearing nanostructured ferritic steels. Acta Mater 2013;61(15):5605–17.

[25] Doñate-Buendia C, Kürnsteiner P, Stern F, Wilms MB, Streubel R, Kusoglu IM, Tenkamp J, Bruder E, Pirch N, Barcikowski S, Durst K, Schleifenbaum JH, Walther F, Gault B, Gökce B. Microstructure formation and mechanical properties of ODS steels built by laser additive manufacturing of nanoparticle coated iron-chromium powders. Acta Mater 2021;206.
[26] Rieken JR, Anderson IE, Kramer MJ, Odette G, Stergar E, Haney E. Reactive gas atomization processing for Fe-based ODS alloys. J Nuclear Mater 2012;428(1–3):65–75.
[27] Liu W, DuPont J. Fabrication of functionally graded TiC/Ti composites by laser engineered net shaping. Scr Mater 2003;48(9):1337–42.
[28] Koh HK, Moo JGS, Sing SL, Yeong WY. Use of fumed silica nanostructured additives in selective laser melting and fabrication of steel matrix nanocomposites. Materials 2022;15(5):1869.
[29] Yin H, Yang J, Zhang Y, Crilly L, Jackson RL, Lou X. Carbon nanotube (CNT) reinforced 316L stainless steel composites made by laser powder bed fusion: microstructure and wear response. Wear 2022;496:204281.
[30] Wang W, Wentz KM, Hayes SE, Johnson DW, Keszler DA. Synthesis of the hydroxide cluster [Al13 (μ3-OH) 6 (μ-OH) 18 (H2O) 24] 15+ from an aqueous solution. Inorg Chem 2011;50(11):4683–5.
[31] Poudel B, Hao Q, Ma Y, Lan Y, Minnich A, Yu B, Yan X, Wang D, Muto A, Vashaee D. High-thermoelectric performance of nanostructured bismuth antimony telluride bulk alloys. Science 2008;320(5876):634–8.
[32] Vafaei S, Purkayastha A, Jain A, Ramanath G, Borca-Tasciuc T. The effect of nanoparticles on the liquid–gas surface tension of Bi2Te3 nanofluids. Nanotechnology 2009;20(18):185702.
[33] Li C, Guo Y, Zhao J. Interfacial phenomena and characteristics between the deposited material and substrate in selective laser melting inconel 625. J Mater Process Technol 2017;243:269–81.
[34] Ghayoor M, Lee K, He Y, Chang C-H, Paul BK, Pasebani S. Selective laser melting of 304L stainless steel: role of volumetric energy density on the microstructure, texture and mechanical properties. Addit Manuf 2020:32.
[35] Yuan P, Gu D. Molten pool behaviour and its physical mechanism during selective laser melting of TiC/AlSi10Mg nanocomposites: simulation and experiments. J Phys D Appl Phys 2015;48(3).
[36] Zhong S, Zuber MT, Moresi L, Gurnis M. Role of temperature-dependent viscosity and surface plates in spherical shell models of mantle convection. J Geophys Res Solid Earth 2000;105(B5):11063–82.
[37] King WE, Barth HD, Castillo VM, Gallegos GF, Gibbs JW, Hahn DE, Kamath C, Rubenchik AM. Observation of keyhole-mode laser melting in laser powder-bed fusion additive manufacturing. J Mater Process Technol 2014;214(12):2915–25.
[38] Dai D, Gu D. Influence of thermodynamics within molten pool on migration and distribution state of reinforcement during selective laser melting of AlN/AlSi10Mg composites. Int J Mach Tool Manuf 2016;100:14–24.
[39] Li XP, Ji G, Chen Z, Addad A, Wu Y, Wang H, Vleugels J, Van Humbeeck J, Kruth J-P. Selective laser melting of nano-TiB2 decorated AlSi10Mg alloy with high fracture strength and ductility. Acta Mater 2017;129:183–93.
[40] Ma C, Zhao J, Cao C, Lin T-C, Li X. Fundamental study on laser interactions with nanoparticles-reinforced metals—part II: effect of nanoparticles on surface tension, viscosity, and laser melting. J Manuf Sci Eng 2016;138(12):121002.
[41] Corcione M. Empirical correlating equations for predicting the effective thermal conductivity and dynamic viscosity of nanofluids. Energ Conver Manage 2011;52(1):789–93.
[42] Rai R, Elmer J, Palmer T, DebRoy T. Heat transfer and fluid flow during keyhole mode laser welding of tantalum, Ti–6Al–4V, 304L stainless steel and vanadium. J Phys D Appl Phys 2007;40(18):5753.
[43] Khairallah SA, Anderson AT, Rubenchik A, King WE. Laser powder-bed fusion additive manufacturing: physics of complex melt flow and formation mechanisms of pores, spatter, and denudation zones. Acta Mater 2016;108:36–45.
[44] Mumtaz K, Hopkinson N. Selective laser melting of thin wall parts using pulse shaping. J Mater Process Technol 2010;210(2):279–87.
[45] Ghayoor M, Lee K, He Y, Chang C-H, Paul BK, Pasebani S. Selective laser melting of austenitic oxide dispersion strengthened steel: processing, microstructural evolution and strengthening mechanisms. Mater Sci Eng A 2020;788.
[46] Boegelein T, Louvis E, Dawson K, Tatlock GJ, Jones AR. Characterisation of a complex thin walled structure fabricated by selective laser melting using a ferritic oxide dispersion strengthened steel. Mater Charact 2016;112:30–40.
[47] Huang G, Wei K, Deng J, Liu M, Zeng X. High-power laser powder bed fusion of 316L stainless steel: defects, microstructure, and mechanical properties. J Manuf Process 2022;83:235–45.
[48] Katancik M, Mirzababaei S, Ghayoor M, Pasebani S. Selective laser melting and tempering of H13 tool steel for rapid tooling applications. J Alloys Compd 2020;849:156319.
[49] Saeidi K, Gao X, Zhong Y, Shen ZJ. Hardened austenite steel with columnar sub-grain structure formed by laser melting. Mater Sci Eng A 2015;625:221–9.
[50] Bertoli US, Guss G, Wu S, Matthews MJ, Schoenung JM. In-situ characterization of laser-powder interaction and cooling rates through high-speed imaging of powder bed fusion additive manufacturing. Mater Des 2017;135:385–96.
[51] Gaskell DR, Laughlin DE. Introduction to the thermodynamics of materials. CRC Press; 2017.
[52] Mirzababaei S, Paul BK, Pasebani S. Microstructure-property relationship in binder jet produced and vacuum sintered 316 L. Addit Manuf 2022;53:102720.
[53] AlMangour B, Grzesiak D, Yang J-M. In-situ formation of novel TiC-particle-reinforced 316L stainless steel bulk-form composites by selective laser melting. J Alloys Compd 2017;706:409–18.
[54] Paul BK, Lee K, He Y, Ghayoor M, Chang C-H, Pasebani S. Oxide dispersion strengthened 304 L stainless steel produced by ink jetting and laser powder bed fusion. CIRP Ann 2020;69(1):193–6.